A new ternary Li_4FeSb_2 structure formed upon discharge of the $FeSb_2$/Li cell

C. Villevieille, B. Fraisse, M. Womes, J.-C. Jumas, L. Monconduit *

Institut Charles Gerhardt, Laboratoire des Agrégats, Interfaces et Matériaux pour l'Energie, Université Montpellier II, Place E. Bataillon, Bat. 15, cc15 34095 Montpellier Cedex 5, France

ABSTRACT

We report here the performance of $FeSb_2$ used as negative electrode for Li-ions batteries. A capacity of $400\,mAh\,g^{-1}$ and $3500\,mAh\,cm^{-3}$ can be retained after 10 cycles at a C/10 cycling rate. We studied in particular the electrochemical mechanism during the first discharge of the $FeSb_2$/Li battery. Both Mössbauer spectroscopy (^{57}Fe and ^{121}Sb) and *in situ* XRD studies show the formation of an unknown *fcc*-phase during the first step. A second step shows the conversion process leading to Li_3Sb at the end of the discharge. The structure of the intermediate new phase Li_4FeSb_2 is isotype to the face-centered-cubic Li_3Sb phase in which one Fe atom is substituted by two Li atoms.

© 2008 Elsevier B.V. All rights reserved.

1. Introduction

In recent years, lithium-ion batteries have become the most important power sources for portable equipment due to their high-specific energy and high-working voltage. Nowadays, Li-ion batteries with the conventional negative electrode material based on carbon graphite ($372\,mAh\,g^{-1}$, $820\,mAh\,cm^{-3}$) cannot face to the increasing demand of energy. The exploration of new materials and the understanding of their electrochemical mechanisms are essential to better control the electrode properties.

Tin alloys belong to the most interesting intermetallic compounds and are thus intensively investigated. Although offering much higher specific capacities than the intercalated carbon-based compounds, these materials unfortunately suffer from unacceptable capacity loss and severe volumetric changes (300%) upon cycling [1–3]. Some Sb-based intermetallic compounds, such as $CoSb_3$ [4,5] and Cu_2Sb [6,7], have been investigated as negative electrodes. Antimonides of the form MSb_2 (M = Cr, Fe, Ni, Co) have attracted particular interest [8–10]. However, whatever the transition metal M, the capacity retention was very poor. The authors

concluded that the reversible capacity was based on the alloying/dealloying of Li with Sb.

More recently we reported the study of the electrochemical reaction mechanism of lithium with $NiSb_2$ prepared by high temperature synthesis [11]. The advantage of as prepared $NiSb_2$, by comparing with other antimonides, does not lie in its high reversible capacity ($520\,mAh\,g^{-1}$, $4080\,mAh\,cm^{-3}$) but rather in its ability to maintain (after the first discharge) 100% of its capacity over 15 cycles as well as on its aptitude to deliver its full capacity at high discharge/charge rates. The performance originates in an original reversible process. During the first discharge, $NiSb_2$ is converted into Li_3Sb and probably Ni^0 nanoparticles. Upon the first charge, the composite electrode ($Li_3Sb + Ni^0$) is transformed to the high-pressure $NiSb_2$ form and Sb. Once the first cycle achieved, the following discharges proceed via a two-step process with, first, the lithiation of Sb leading to Li_2Sb, followed by the conversion reaction of $NiSb_2$-HP to $2Li_3Sb + Ni^0$ [12].

We decided to explore the electrochemical mechanism of the marcasite $FeSb_2$ phase, which presents the same marcasite-type structure as $NiSb_2$ [13]. The aim is to compare the reactivity of the marcasite MSb_2 phase versus Li, when M is iron or nickel. From electrochemical studies, *in situ* XRD, ^{121}Sb and ^{57}Fe Mössbauer measurements we demonstrate in this paper that an original mechanism takes place with the formation of a new ternary phase Li_4FeSb_2 during the first part of the discharge. Since no Li/Fe/Sb

* Corresponding author. Tel.: +33 467 14 33 35; fax: +33 467 14 33 04.
E-mail address: laure.monconduit@univ-montp2.fr (L. Monconduit).
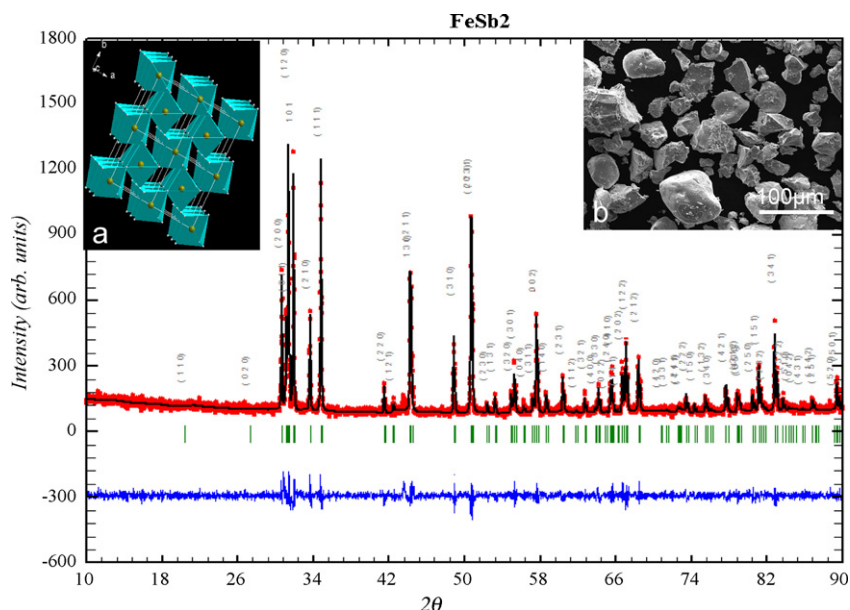
Fig. 1. X-ray diffraction patterns (Cu Kα) of the orthorhombic FeSb$_2$ phase prepared by a high temperature ceramic route. Insets show the marcasite structure of FeSb$_2$ (a) and the SEM image (b). (For interpretation of the references to colour in this figure legend, the reader is referred to the web version of the article.)

phase is described in the literature, we present here this new phase.

2. Experimental

2.1. Synthesis and characterization

The orthorhombic FeSb$_2$ phase was obtained by placing stoichiometric amount of iron metal and antimony powders in a silica tube sealed under vacuum. The silica tube was placed in a furnace and heated to 730 °C during 4 days using a ramp of 2 °C min^{-1}. The tube was then air quenched. Powder X-ray diffraction (Fig. 1) revealed well-shaped Bragg peaks, indicative of a highly crystalline sample.

2.2. Electrochemical tests

Swagelok-type cells were assembled in an argon filled glove box and cycled using a Mac Pile automatic cycling/data recording systems (Biologic Co., Claix, France) in a potential window between 2 V and 0.01 V versus Li$^+$/Li^0 at a cycling rate of C/n (that is one lithium per formula unit within n hours). These cells comprised a Li metal disc as the negative electrode, a Whatman GF/D borosilicate glass fiber sheet saturated with a 1-M LiPF$_6$ in ethylene carbonate (EC), dimethyl carbonate (DMC) (1:1, in w/w) as the electrolyte, a positive electrode made after mixing the starting iron antimonide powder with 15 wt% carbon black (SP). Usually, 10–12 mg of the mixed powders was placed on top of the Swagelok plunger.

2.3. XRD and SEM

X-ray diffraction (XRD) measurements on powdered FeSb$_2$ samples were performed on a Philips X-pert diffractometer using Cu Kα radiation. *In situ* XRD was carried out on electrochemical cell assembled similarly to our Swagelok cells but with a beryllium window as current collector on the X-ray side. The cell was discharged at a C/10 scan rate and the X-ray powder patterns were collected for every 0.5 reacted Li. The powder morphology of pristine materials

was determined by scanning electron microscopy (SEM) coupled with energy-dispersive X-ray spectroscopy (EDX).

2.4. Mössbauer spectroscopy

[121]Sb Mössbauer measurements were performed on an EG and G constant acceleration spectrometer in transmission mode using a Ba[121m]SnO$_3$ source of a nominal activity of 0.2 mCi. During the measurements, both source and absorbers were simultaneously cooled down to 4 K in order to increase the fraction of recoil-free absorption and emission processes. The zero isomer shift was defined from the spectrum of InSb at 4 K ($\delta = -8.72(4)$ mm s^{-1} relative to the source). Measurements were performed *ex situ* at several depths of discharge.

[57]Fe Mössbauer spectra were recorded in transmission geometry in the constant acceleration mode, using equipment supplied by Ortec and Wissel and a [57]Co(Rh) source of a nominal activity of 10 mCi. The velocity scale was calibrated by means of a room temperature spectrum of α-Fe. Isomer shifts are given with respect to the room temperature spectrum of α-Fe.

The hyperfine parameters isomer shift and quadrupole splitting were determined by fitting Lorentzian lines to the experimental data, using appropriate computer programs [14,15].

3. Results

Fig. 1 shows the Rietveld refinement of the powder pattern of the as-obtained FeSb$_2$. All peaks can be indexed on the basis of an orthorhombic (marcasite-type) cell with refined lattice parameters ($a = 5.829(2)$ Å; $b = 6.535(1)$ Å; $c = 3.197(1)$ Å) similar to those reported in the literature. Note that in the literature the FeSb$_2$ crystallographic structure is indexed in two space groups, *Pnn2* (34) and *Pmnn* (58) [16,17]. Both structures are essentially of the FeS$_2$-m type, the *Pnn2* space group lacks, however, a mirror plane present in the structure of FeS$_2$-m, due to a slight shift of the Sb atoms along the *z*-direction. As a consequence, the Fe atoms in *Pnn2* are no longer situated in the center of the Sb$_6$ octahedra (see Table 1).

In the classical marcasite type structure, each Fe is octahedrally coordinated to six nearest Sb atoms and each Sb atom is

| Sb atomic position	x	y	z
Pnn2	0.1881 (1)	0.3565 (1)	0.0097 (5)
Pmnn	0.1885 (2)	0.3561 (4)	0.000

tetrahedrally surrounded by three Fe and one Sb. The reduction of the symmetry in *Pnn2* of the Fe atoms leads to three non-equivalent Fe–Sb bonding distances, each occurring twice per Fe–Sb octahedron. This compound has a predominantly covalent type of bonding. Like other antimonide compounds with marcasite structure, FeSb$_2$ behaves as a semiconductor.

The left inset of Fig. 1, shows the SEM picture of the FeSb$_2$ powder. As expected for this type of synthesis, the powder morphology shows agglomerates of 20–50 μm. EDX analyses give systematically the expected 2Sb/1Fe molar ratio.

3.1. Electrochemical tests

The FeSb$_2$/Li half-cells were tested using different C/n rates ($n = 1$; 3; 10; 20). For the sake of clarity, only the first three half-cycles are shown in Fig. 2 (on the left). The best performance is obtained for a C/10 cycling rate. At this rate, more than 6 Li per formula unit react during the first discharge. On charge, only 4.5 Li are removed corresponding to a reversible capacity of 420 mAh g^{-1} (or 3500 mAh cm^{-3}). The galvanostatic curve shows a voltage plateau at 0.62 V during the first discharge, which is correlated to the reaction of more than 4 Li. The corresponding incremental peak (labelled A, at 0.65 V) is sharp, suggesting a two-phase reaction (grey line in Fig. 3). A second step occurs at 0.4 V, which corresponds to the insertion of only 1.5 Li. On charge, a double process (B′/A′) appears between 0.9 V and 1.1 V, which is clearly viewed on the derivative curve on Fig. 3.

The profile of the second discharge is very different with a very huge peak centered at 0.87 V and two sharp peaks at 0.84 V and 0.9 V
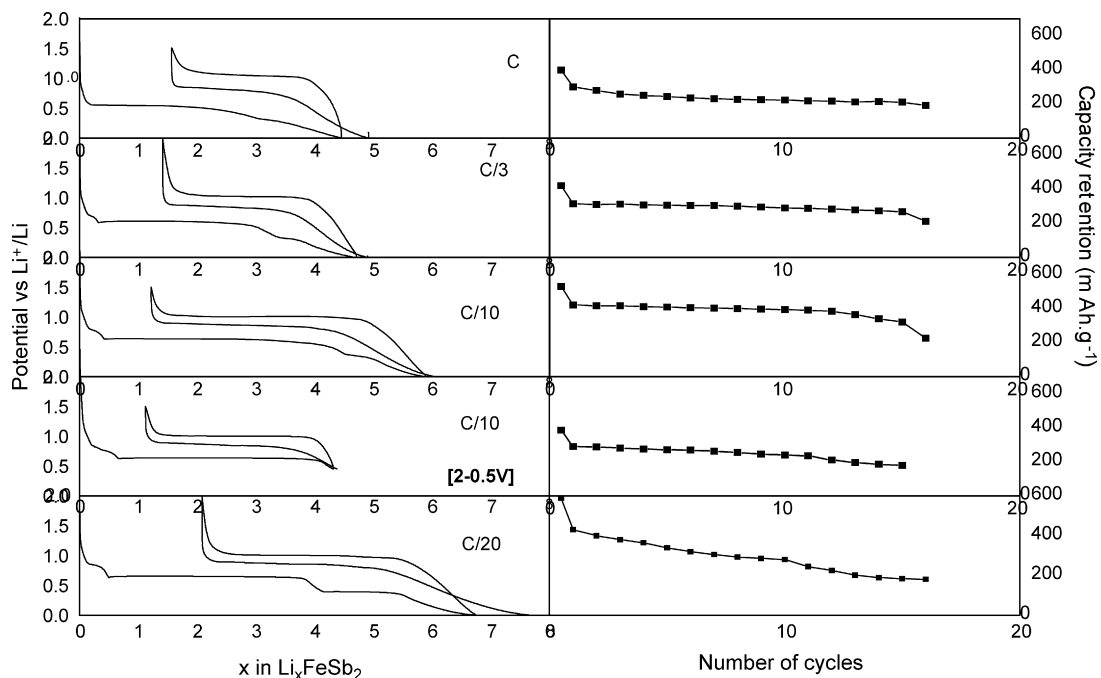
Fig. 2. Voltage vs. composition plots for a FeSb$_2$/Li cell between 2 V and 0 V or between 2 V and 0.5 V, cycled at C; C/3; C/10; C/20 and the corresponding capacity retention.
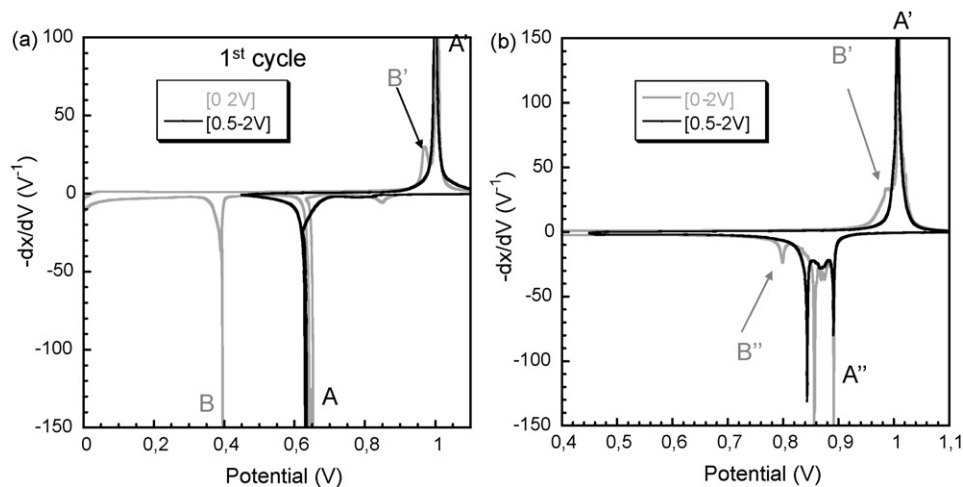
Fig. 3. Plots of the derivatives −dx/dV (a) of the first and (b) of the second cycles of a FeSb$_2$/Li cell at a C/20 rate between 2 V and 0 V (in grey line) and between 2 V and 0.5 V (in black line).
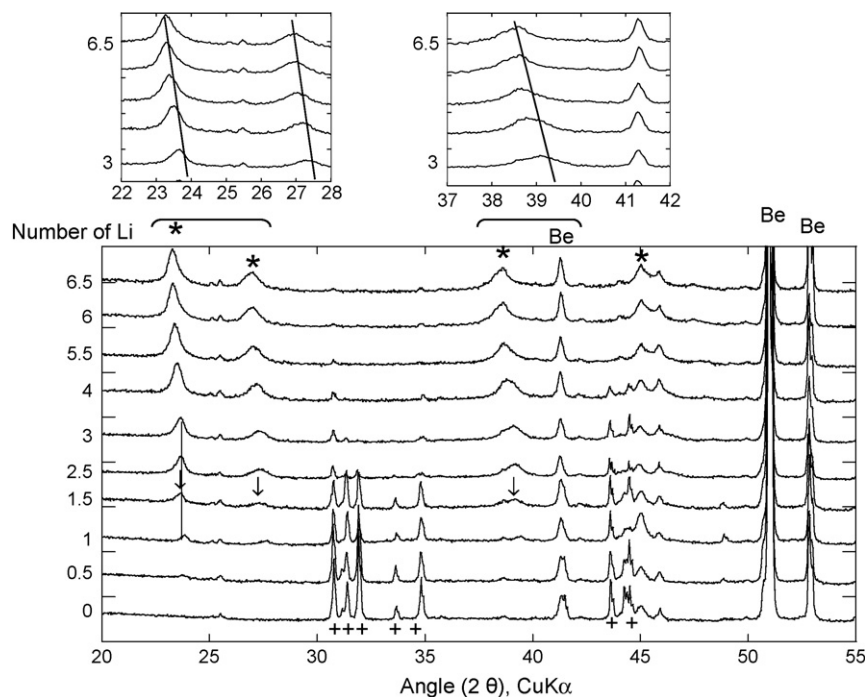
Fig. 4. *In situ* X-ray diffraction patterns recorded during the discharge of a FeSb$_2$/Li electrochemical cell down to 0 V at a C/10 cycling rate. The Bragg peaks corresponding to m-FeSb$_2$ phase, to the Li$_4$FeSb$_2$ phase (or phase 1), and to the Li$_3$Sb phase (or phase 2) are marked by crosses, arrows and black stars, respectively.

(this block of peaks is labelled A″). A smaller B″ peak is observed at 0.8 V. When a potential cut off is applied at 0.5 V, the B process is no more observed on first discharge. As a consequence both B′ and B″ processes disappear on successive charge and discharge, respectively.

At higher rate (C or C/3), only 3 Li per formula unit react reversibly during the first cycle, which corresponds to a reversible capacity of 300 mAh g^{-1}. At a very low rate (C/20), the reversible capacity of the first cycle increases significantly (5.5 Li corresponding to 610 mAh g^{-1}). Simultaneously, the irreversible part of the first cycle increases, too. Note that in this case the second process at 0.4 V is correlated with the reaction of 2 Li.

Whatever the cycling rate is, the FeSb$_2$/Li cell shows a very reproducible voltage profile upon subsequent cycles but suffers from an important capacity fading after 15 cycles (Fig. 2, on the right). The best capacity retention is obtained at a C/10 cycling rate, with a capacity of 400 mAh g^{-1} measured after 10 cycles. Note that the cycleability is not improved when the 0.5 V cut-off is applied (Fig. 2).

In order to gain deeper insight in the electrochemical mechanism, both *in situ* XRD and Mössbauer spectroscopy measurements (^{121}Sb and ^{57}Fe) were collected at selected potential points during the first discharge. The first XRD pattern at 0 Li corresponds to the starting FeSb$_2$ phase recorded in the *in situ* XRD cell with the Beryllium window as current collector. During the first discharge (Fig. 4), we initially observe a continuous decrease in the intensity of the main FeSb$_2$ Bragg peaks to the expense of a new set of Bragg peaks (phase 1) marked by arrows in Fig. 4. These peaks then continuously grow upon increasing x up to x = 4. Pursuing the lithiation results in a continuous shift of this new set of broad peaks to lower angles (phase 2). Table 2 summarizes the Bragg peaks observed for phase 1 and for phase 2 together with the corresponding cell parameters, both refined in *Fm3m* space group. At the end of discharge the set of peaks of phase 2 can be attributed to the main Bragg peak of the cubic Li$_3$Sb phase (a = 6.572 Å, Fm3m) [18]. Note that the face-centered-cubic Li$_3$Sb phase is designated in the Li/Sb phase diagram as the high temperature polyform (the ambient

temperature α-Li$_3$Sb transforms to β-Li$_3$Sb at temperatures above 650 °C).

At the end of the discharge, the diffuse peak around 45° could also be interpreted as the (1 1 0) Bragg peak of the cubic iron phase (JCPDF 01-1252).

3.2. Mössbauer study

A ^{121}Sb and ^{57}Fe Mössbauer study was undertaken in order to better identify the intermediate phases formed during the discharge in the electrode and in particular the ternary Li/Fe/Sb phase.

The ^{121}Sb and the ^{57}Fe Mössbauer spectra are shown in Fig. 5 and the corresponding refined hyperfine parameters are included in Tables 3a and 3b. Note that ^{121}Sb isomer shifts in Table 3b are given relative to InSb, while the velocity scale in Fig. 5 is drawn relative to the source (InSn on this scale would be at δ = −8.72 mm s^{-1}). For the starting material, the ^{57}Fe spectral shape reveals two doublets. The hyperfine parameters of the first doublet (σ = 0.44 mm s^{-1}; ΔE$_q$ = 1.22 mm s^{-1} and 85% relative contribution) agree well with the published data for the orthorhombic FeSb$_2$ phase (σ = 0.44 mm s^{-1} and ΔE$_q$ = 1.27 mm s^{-1}) [19]. However, the second doublet (σ = 0.39 mm s^{-1}; ΔE$_q$ = 0.5 mm s^{-1} and

Table 2
Bragg peaks of the fcc-Li$_3$Sb according to the literature, of Phase 1 observed during the first discharge, and of Phase 2 at the end of the discharge

	Li$_3$Sb fcc [16]	Phase 1	Phase 2
Bragg peaks	23.47	23.9	23.3
2θ	27.08	27.7	27.0
	38.79	39.4	38.7
	45.78	45.9	45.85
	47.85	47.44	/
Refined cell parameters (Å)	a = 6.572	a$_1$ = 6.28	a$_2$ = 6.56
Cell volume (Å^3)	V = 283.8	V$_1$ = 247.67	V$_2$ = 282.30

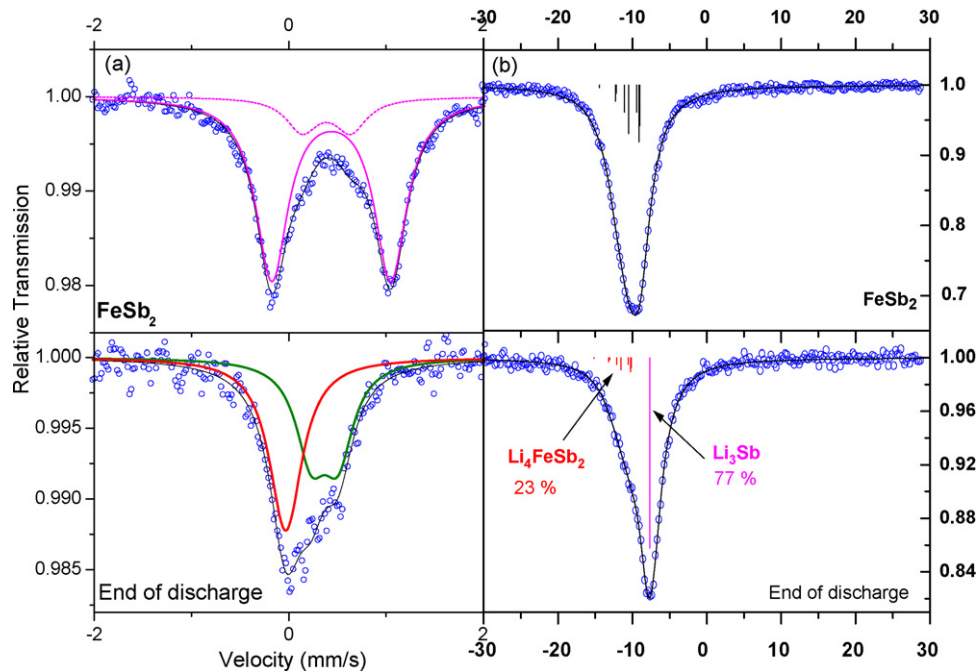**Fig. 5.** (a) ^{57}Fe and (b) ^{121}Sb Mössbauer spectra of a FeSb$_2$/Li starting electrode and of a fully discharged electrode.

Table 3a
^{57}Fe hyperfine parameters of FeSb$_2$; δ isomer shift relative to α-Fe; ΔEq, quadrupole splitting; Γ, line width at half maximum; A, contribution of the spectrum

		δ (mm s^{-1})	Δq (mm s^{-1})	Γ (mm s^{-1})	A (%)
FeSb$_2$	^{57}Fe	0.44 (3)	1.22 (8)	0.40 (1)	84.5
		0.39 (2)	0.50 (2)	0.40 (1)	15.5
(End of 1st discharge)	^{57}Fe	−0.03 (1)	0.00(0)	0.41 (2)	50.8
		0.37 (2)	0.28 (2)	0.38 (3)	49.2

15% relative contribution) does not correspond to any phase in the literature. Note that no trace of another FeSb$_2$ phase has been distinguished by XRD (Fig. 1) and in the Rietveld refinement. The second spectrum, recorded at the end of the discharge, shows a singlet (red colour) and a doublet (green colour) with very close relative contributions (51% and 49%, respectively). The singlet, appearing at zero velocity, can be attributed to small particles of metallic iron, showing superparamagnetic behaviour as it is characteristic for particle diameters of the order of a few nanometers. The hyperfine parameters of the doublet are quite similar to the second doublet of the starting material and might reflect an incomplete reaction of the pristine material or the presence of the new ternary phase.

The ^{121}Sb spectrum of the starting either material is characterized by a multiplet with the hyperfine parameters ($\sigma = -1.35$ mm s^{-1}; $eQV_{zz} = 11$ mm s^{-1} and 100% relative contribution) in good agreement with the data related to FeSb$_2$ in the literature [20]. At the end of the discharge, two contribu-

Table 3b
^{121}Sb hyperfine parameters of FeSb$_2$; δ isomer shift relative to InSb; eQV_{zz} quadrupole splitting; Γ, line width at half maximum; A, contribution of the spectrum

|		δ (mm s^{-1})	eQV_{zz} (mm s^{-1})	Γ (mm s^{-1})	A (%)
FeSb$_2$	^{121}Sb	−1.35 (1)	+11.0 (2)	1.60 (3)	100
(End of 1st discharge)	^{121}Sb	−2.41 (9)	+10 (1)	1.79 (6)	23.0
		+1.05 (3)	0.0	1.79 (6)	77.0

tions appear. The refined parameters of the first ($\sigma = 1.05$ mm s^{-1}; $eQV_{zz} = 0$ mm s^{-1} and 77% relative contribution) are ascribable to the fcc-Li$_3$Sb phase [21]. The second component is characterized by a multiplet with the hyperfine parameters $\sigma = -2.41$ mm s^{-1}; $eQV_{zz} = 10$ mm s^{-1} and 23% relative contribution). This new contribution is not described in the literature. The zero quadrupole interaction of Sb in Li$_3$Sb is in agreement with the perfect cubic symmetry of the antimony sites in this compound, where Sb atoms are surrounded by 8 Li atoms at a distance 2.7 Å, situated in the corners of a cube, and by 6 Li forming a regular octahedron with a Sb–Li distance of 3.1 Å (see Fig. 6). In the ternary phase, the local environment of Sb is the same as in Li$_3$Sb with the exception of Fe atoms substituting for Li on the corners of the cube in statistical distribution. The different ionic diameters of Li and Fe and the different Li–Sb and Fe–Sb bonding properties induce a distortion of the ideal cubic symmetry of the antimony site and lead to a non-zero quadrupolar interaction.

4. Discussion

Two electrochemical processes, A and B, were observed during the first discharge. *In situ* XRD showed that during the first A process (4 Li), the starting FeSb$_2$ phase progressively disappears to the benefit of the phase 1. All their diffraction peaks correspond to the characteristic X-ray pattern of the cubic Li$_3$Sb phase, but are shifted to higher angles. A cubic cell parameter was calculated as $a = 6.28$ Å for this phase 1 (see Table 4). The broad peak at 45° is tentatively attributed to the (1 1 0) reflexion of the cubic Fe phase. Depending on the correctness of this attribution, the chemical composition of this new phase 1 is either Li$_4$FeSb$_2$ or Li$_4$Fe$_{1-x}$Sb$_2$. Note that no phase is described in the Li/Fe/Sb system in the literature. In all cases this phase 1 appears to be isostructural of Li$_3$Sb.

As already emphasized above, the Fe atoms in FeSb$_2$ are octahedrally coordinated to six Sb atoms and each Sb atom is surrounded by three near Fe and one near Sb in a tetrahedral configuration, leading to three non-equivalent bonding Fe–Sb distances, to one Fe–Fe distance and three Sb–Sb distances. These distances are reported in
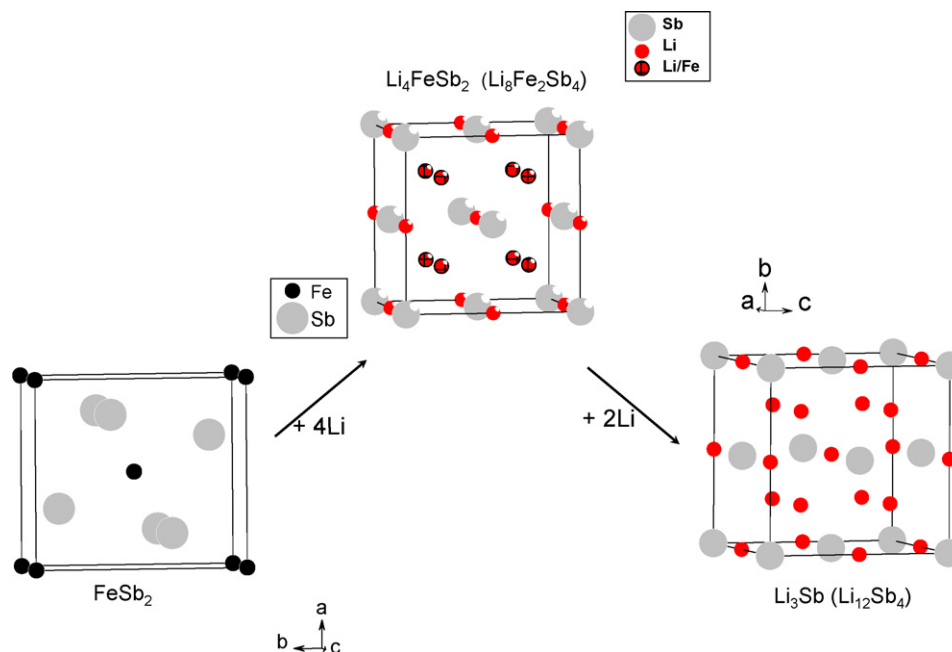
Fig. 6. Crystallographic structures of FeSb$_2$, Li$_4$FeSb$_2$ and Li$_3$Sb, showing the positions of Fe (black), Sb (grey) and Li (red). (For interpretation of the references to colour in this figure legend, the reader is referred to the web version of the article.)

Table 4 with the corresponding distances in the new ternary phase 1 and in Li$_3$Sb.

As shown in Fig. 6, the structure of Li$_4$FeSb$_2$ is isotype with that of Li$_3$Sb, with one Fe^{II} atom substituting for two Li on the tetrahedral 8c site. This structural description was validated by the Mössbauer analysis. In contrast to that, no such close structural relationship exists between the antifluorine type structure Li$_4$FeSb$_2$ and FeSb$_2$. The FeSb$_2$ → Li$_4$FeSb$_2$ phase transformation involves structural modifications with shortening or lengthening of the Fe–Fe, Fe–Sb and Li–Sb distances. Accordingly, the electrochemical analysis shows that process A is characterized by a biphasic process. In contrast to this, process B, i.e. the transformation from Li$_4$FeSb$_2$ to Li$_3$Sb, does not imply modifications of the array of Sb atoms and can be seen as a topotactic displacement. The continuous shift of the Bragg peaks during the discharge from $x = 4$ to $x = 6$ confirms this hypothesis. The Li$_4$FeSb$_2$ → Li$_3$Sb transformation involves an increase in the lattice parameter of 4.5% and in the volume cell of 14%. This increase of the cell parameters is due to the more covalent character of the Fe–Sb bonds as compared to the more ionic character of the Li–Sb bonds in Li$_3$Sb. This degree of covalency of the transition metal (TM)–pnictogen bond has been widely observed in the ternary phosphide antifluorine-type structures [22,23].
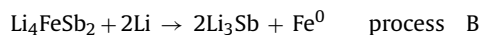
It is interesting to note that Li/TM/Sb phases are very rare. Only the *fcc* Li$_2$CuSb phase is reported with a cell parameter ($a = 6.27$ Å) [24] which is very close to that of phase 1.

Moreover, the *fcc* Li$_2$CuSb was recently identified as being an intermediate phase in the discharge of the Cu$_2$Sb/Li half-cell [6,7].

In this case, the successive Cu$_2$Sb → Li$_2$CuSb and Li$_2$CuSb → Li$_3$Sb transformations were observed during the first discharge. The extruded copper was not characterized by XRD, but only by selected area electron diffraction (SAED) analysis. The Li$_2$CuSb → Li$_3$Sb transition led to an increase in the lattice parameter of 4.5%, corresponding to a 14% expansion of the cubic lattice. We observed exactly the same volume variation from Li$_4$FeSb$_2$ to Li$_3$Sb, meaning that the same type of electrochemical reaction takes place.

5. Conclusion

This combined ^{57}Fe and ^{121}Sb Mössbauer spectroscopy and *in situ* XRD analysis showed that a two-step mechanism takes place during the first discharge of the FeSb$_2$/Li cell:

$$FeSb_2 + 4Li \rightarrow Li_4FeSb_2(or\ Li_4Fe_{1-x}Sb_2 + xFe^0) \qquad process\ A$$

$$Li_4FeSb_2 + 2Li \rightarrow 2Li_3Sb + Fe^0 \qquad process\ B$$

Li$_4$FeSb$_2$ is a new crystallographic structure, since no Li/Fe/Sb phase was ever referenced in the literature. Although two steps clearly appear in the voltage profiles of previous articles reporting the FeSb$_2$ behaviour versus Li, no explanation was ever given by the authors about it [9,10]. Low temperature Mössbauer measurements are currently in progress to confirm the presence of metallic iron particles in the fully discharged electrodes and eventually in the electrode collected during the first A process. Moreover, the analysis

Table 4
cell parameters and interatomic distances in the FeSb$_2$, Phase 1 and Li$_3$Sb

	Refined cell parameters Å and volume cell Å^3	Fe/Li–Sb (Å)	(Li/Fe)–(Li/Fe) (Å)	Sb–Sb (Å)
FeSb$_2$ (*Pnn2*)	$a = 5.829(2)$; $b = 6.535(1)$; $c = 3.197(1)$; $V = 121.78$	2.576; 2.578; 2.616	3.197	2.887(1); 3.197(1); 3.606(1)
Li$_4$FeSb$_2$; $Z = 2$; (=Li$_8$Fe$_2$Sb$_4$; $Z = 1$); (*Fm-3m*)	$a = 6.28$; $V = 247.67$	2.719(Fe/Li–Sb); 3.14 (Li–Sb)	2.719 (Li–Li/Fe); 3.14 (Li/Fe–Li/Fe); 4.441 (Li–Li)	4.44
Li$_3$Sb; $Z = 4$; (=Li$_{12}$Sb$_4$; $Z = 1$); (*Fm-3m*)	$a = 6.56$; $V = 282.30$	2.84; 3.28	2.84; 3.28; 4.638	4.638

of the samples collected on charge of the $FeSb_2$/Li battery will show (i) whether the $Li_4FeSb_2 \rightarrow Li_3Sb$ is reversible and (ii) whether $FeSb_2$ is restructured from Li_4FeSb_2 at the end of charge.

References

[1] I. Rom, M. Wachtler, I. Papst, M. Schmied, J.O. Besenhard, F. Hofer, M. Winter, Solid State Ionics 143 (3–4) (2001) 329.
[2] Y. Hamon, T. Brousse, F. Jousse, P. Topart, P. Buvat, D.M. Schleich, J. Power Sources 96–97 (2001) 185.
[3] S. Naille, C.M. Ionica-Bousquet, F. Robert, F. Morato, P.-E. Lippens, J. Olivier-Fourcade, J. Power Sources 174 (2007) 1091.
[4] R. Alcantara, F.J. Fernandez-Madrigal, P. Lavela, J.L. Tirado, J.C. Jumas, J. Olivier-Fourcade, J. Mater. Chem. 9 (1999) 2517.
[5] C.M. Ionica, L. Aldon, P.E. Lippens, F. Morato, J. Olivier-Fourcade, J.-C. Jumas, Hyperfine Interact. 156/157 (2004) 555.
[6] L.M.L. Fransson, J.T. Vaughey, R. Benedek, K. Edström, J.O. Thomas, M.M. Thackeray, Electrochem. Commun. 3 (2001) 317.
[7] M. Morcrette, D. Larcher, J.M. Tarascon, K. Edström, J.T. Vaughey, M.M. Thackeray, Electrochim. Acta 52 (2007) 5339.
[8] F.J. Fernandez-Madrigal, P. Lavela, C. Perez-Vicente, J.L. Tirado, J. Electroanal. Chem. 501 (2001) 205.
[9] J. Xie, X. Zhao, G. Cao, M. Zhao, Y. Zhong, J. Mater. Sci. Technol. 20 (3) (2004) 344.
[10] J. Xie, X. Zhao, G. Cao, M. Zhao, Y. Zhong, L.Z. Deng, Mater. Lett. 57 (2003) 4373.
[11] C. Villevieille, C.M. Ionica-Bousquet, B. Ducourant, J.C. Jumas, L. Monconduit, J. Power Sources 172 (1) (2007) 388.
[12] C. Villevieille, C.M. Ionica-Bousquet, J.C. Jumas, L. Monconduit, Hyperfine Interact., in press.
[13] A. Kjekshus, P.G. Peterzens, T. Rakke, A.F. Andresen, Acta Chim. Scand. A33 (1979) 469.
[14] W. Kündig, Nucl. Instr. Methods 75 (1967) 336.
[15] K. Rubenbauer, T. Birchall, Hyperfine Interact. 7 (1979) 125.
[16] H. Holseth, A. Kjekshus, Acta Chim. Scand. 23 (1969) 3043.
[17] G. Hagg, Nova Acta Regiae Soc. Sci. Ups. 7 (1929) 87.
[18] G. Brauer, E. Zintl, Z. Phys. Chem. (Leipzig) 37 (1937) 323.
[19] J. Steger, E. Kostiner, J. Solid State Chem. 5 (1972) 131.
[20] J.D. Donalson, A. Kjekshus, D.G. Nicholson, M.J. Tricker, Acta Chim. Scand. A26 (1972) 3215.
[21] L. Aldon, A. Garcia, J. Olivier-Fourcade, J.-C. Jumas, F.J. Fernandez-Madrigal, P. Lavela, C. Perez Vicente, J.L. Tirado, J. Power Sources 119 (2003) 585.
[22] F. Gillot, Ph.D. Thesis, University of Montpellier (2003).
[23] M.L. Doublet, F. Lemoigno, F. Gillot, L. Monconduit, Chem. Mater. 14 (2002) 4126.
[24] H. Pauly, A. Weiss, H. Witte, Z. Metallkd. 59 (1968) 47.